Optimization design and test of vibration components in a Chinese wolfberry harvester

Zhicheng Tian[1], Song Mei[2*], Zhiyu Song[2], Cheng Shen[2], Chenghao Pan[1], Yifei Tong[1]
(1. *School of Mechanical Engineering, Nanjing University of Science and Technology, Nanjing 210094, China*;
2. *Nanjing Institute of Agricultural Mechanization, Ministry of Agriculture and Rural Affairs, Nanjing 210014, China*)

Abstract: Linear reciprocating vibration components in Chinese wolfberry harvesters are susceptible to fractures and exhibit high power consumption relative to operational loads. To enhance the operational performance of the vibration apparatus, comprehensive optimization research was conducted on the vibration components. First, a cantilever beam force and stress analysis model was developed based on the structural composition characteristics of vibration components. Simulations under both no-load and load conditions were performed using Abaqus software. Comparing theoretical and simulation results identified stress concentration points, confirming the model's accuracy and indicating that steel is the ideal material for the slider. Next, topology optimization of the steel slider using Abaqus resulted in a 38.61% weight reduction while maintaining the required strength. Finally, Matlab calculations revealed that the maximum torque of the vibration component before and after optimization under no-load conditions was 0.52 N·m and 0.42 N·m, respectively, leading to a 19.23% reduction in power consumption. Torque detection tests conducted using a custom-built torque measurement platform indicated that under no-load conditions, the maximum torque before and after optimization was 0.57 N·m and 0.43 N·m, corresponding to a 24.56% reduction in power consumption. Under a 180 g maximum load, the maximum torque was 0.83 N·m and 0.69 N·m, resulting in a 16.87% reduction in power consumption. The driving torque decreased as the operating position increased and increased with higher branch mass. By fitting the relationship between the correction factor k_2 and the load m_4, a torque correction model under load conditions was obtained. Furthermore, an energy consumption correction model was established, providing a scientific basis for motor selection and operational energy efficiency optimization, and serving as a valuable reference for the development of vibration harvesting components.

Keywords: Chinese wolfberry, reciprocating vibration component, stress analysis, torque, power consumption
DOI: 10.25165/j.ijabe.20251806.10008

Citation: Tian Z C, Mei S, Song Z Y, Shen C, Pan C H, Tong Y F. Optimization design and test of vibration components in a Chinese wolfberry harvester. Int J Agric & Biol Eng, 2025; 18(6): 94–103.

1 Introduction

Chinese wolfberry, a Solanaceae plant characterized by strong seasonality and staggered ripening, is a distinctive economic crop widely cultivated in Northwest China. It demonstrates high adaptability and resistance to drought and salinity-alkalinity. As both a medicinal and edible plant, Chinese wolfberry possesses significant pharmacological and health-promoting properties, and can also be used in wine and beverage production[1]. In recent years, it has attracted increasing attention in both domestic and international markets. With the continuous expansion of Chinese wolfberry cultivation and the large-scale transfer of agricultural labor to non-agricultural sectors, the mechanization of its harvesting and processing has become increasingly critical[2]. Among various harvesting methods, vibration-based harvesting is currently considered the most ideal approach for Chinese wolfberry, as it causes minimal damage to surrounding branches and stems[3]. Currently a considerable body of research has been conducted on the vibration-based harvesting of fruits such as Chinese wolfberry, walnut, and apple, focusing mainly on optimizing parameters such as resonant frequency, vibration duration, amplitude, and excitation position[4-6]. Most of these studies aim to improve vibration efficiency and determine appropriate working parameters for the equipment[7-9]. However, these studies overlook the long-term efficiency and reliability of key components under operational conditions. Consequently, there remains a research gap concerning fatigue failure and energy consumption of core components. In vibration-based Chinese wolfberry harvesting equipment, critical components are subjected to dynamic excitation from the transmission system as well as impact loads, which may lead to decreased operational stability and reduced service life. Therefore, it is imperative to perform lightweight design optimization on reciprocating vibration components to mitigate adverse effects caused by vibration and to enhance the overall performance of the harvesting machinery.

The lightweight design of key components in industrial or agricultural products is widely studied worldwide[10-12]. For example, Lu[13] optimized the planetary gear transmission system of an electric-driven hose reel irrigation machine using Matlab. The results showed a 17.9% reduction in the overall volume of the transmission system and an approximately 25% increase in transmission efficiency. Besides, most lightweight design studies adopt finite

Received date: 2025-07-06 **Accepted date:** 2025-09-12
Biographies: Zhicheng Tian, PhD candidate, research interest: agricultural equipment engineering, agriculture robot, Email: tianzhicheng@njust.edu.cn; **Zhiyu Song**, Researcher, research interest: agricultural mechanization engineering, Email: songzhiyu@caas.cn; **Cheng Shen**, Associate Professor, research interest: agricultural engineering, Email: shencheng@caas.cn; **Chenghao Pan**, MS candidate, research interest: agricultural equipment engineering, Email: 940651303@qq.com; **Yifei Tong**, Professor, research interest: intelligent agriculture, Email: tyf51129@aliyun.com.
***Corresponding author: Song Mei**, Associate Researcher, research interest: agricultural mechanization engineering for fruits. Nanjing Institute of Agricultural Mechanization, Ministry of Agriculture and Rural Affairs, Nanjing 210014, China. Tel: +86-15366092940, Email: meisong@caas.cn.

element methods (FEM) for structural optimization and perform comparative analysis to evaluate the improvements[14,15]. Zhao et al.[16] applied a coupled discrete element and finite element approach to analyze the stress–strain conditions of a straw crusher rotor under load, and conducted topology optimization while maintaining the rotor's maximum stiffness. The optimized rotor reduced mass by 17.19%, while maintaining uniform stress distribution and meeting strength and stiffness requirements. Similarly, Liu et al.[17] carried out lightweight optimization of a ground wheel mechanism using FEM software. The optimization reduced the mass of the auxiliary and multi-purpose ground wheels by 26.72% and 10.96%, respectively, while satisfying strength and stiffness criteria. In addition to structural optimization, the development of energy consumption models for critical components is another key area of concern in agricultural machinery research[18-20]. Xiao et al.[21] investigated the power consumption model of the cutting system in a sugarcane harvester. Using a modular approach and ANSYS/Ls-Dyna, they performed numerical simulations of the cutting process and identified optimal cutting parameters. The lowest power consumption of 0.80 kW was achieved under the conditions of a linear cutting speed of 38.8 m/s, a blade disc tilt angle of 11.66°, and a blade edge angle of 25°. Liu et al.[22] developed a rotary tillage power consumption calculation model for a rapeseed direct-seeding machine based on classical mechanics, analyzing the relationship between rotary tillage power consumption and the machine's motion parameters. EDEM was used to simulate and model the rotary tillage process, and the simulation results were consistent with the theoretical findings. Zhu et al.[23] established a rotary tillage power consumption prediction model for rice field tillage based on the discrete element method, applicable to various rotary tillage blades and working conditions. The field test results showed a power consumption prediction error range of 2.50% to 12.81%, indicating that the model has high accuracy. In summary, existing research focuses on analyzing component performance enhancement and energy efficiency reduction. This study aims to perform a lightweight design of the vibration components in Chinese wolfberry harvesters, while taking into account structural strength, welding processes, and low power consumption requirements.

The vibration component is an integrated beam structure formed by the bolted hinge connection of alloy steel fork rods, nylon base connectors, and sliders. In selecting slider materials between aluminum alloy and steel, fatigue tests revealed that aluminum alloy sliders tend to fracture at the cantilever and hinge junctions under prolonged high-frequency vibration, rendering them unsuitable for extended operational cycles. Although steel sliders exhibit superior overall strength, stress concentrations at welded joints can still induce localized failures. These findings highlight the existing reliability issues in material selection and structural design of vibration components, and indicate a lack of systematic optimization concerning inertial loads and power consumption characteristics, thereby constraining the overall operational performance of vibration-based harvesting equipment. Therefore, this study addresses issues such as stress concentration, fatigue failure, and high power consumption that arise during the operation of the vibration components. A comprehensive approach combining theoretical modeling, Abaqus simulation analysis, and experimental validation is used to systematically investigate the vibration components from the perspectives of stress distribution, torque variation, and energy consumption characteristics. The focus is on achieving lightweight optimization of the slider through topology optimization. Additionally, a high-frequency torque detection system is employed to obtain the actual power output values of the optimized vibration components, providing a basis for model correction and accurate motor selection.

2 Theoretical analysis

2.1 Theoretical stress analysis of the reciprocating vibration component

Based on the operational characteristics of the reciprocating vibration mechanism, the primary structure of the reciprocating vibration component is extracted as shown in Figure 1. In the theoretical analysis, considering that the operation involves high-frequency and small-amplitude vibrations, the vibration frequency is much higher than the static deformation caused by gravity. The magnitude of the inertial forces is significantly greater than that of gravity, and the direction of gravity is orthogonal to the primary direction of motion. Therefore, the effect of gravity on stress distribution and deformation can be neglected. Only the cantilever beam stress analysis under the periodic inertial force is considered, as shown in Figure 2a. Here, P_1 denotes the inertial force at the center of mass of the slider; P_2 represents the resultant inertial force acting on the combined mass and center of mass of the extended steel component, nylon base, and U-shaped fork rod welded to the slider; and P_z is the total inertial force corresponding to the entire mass and center of mass of the vibration component. All inertial forces are assumed to act in the direction of reciprocating motion along the x-axis, while the influence of gravitational force in the vertical direction is considered negligible. For the slider component with length l_1, the root section possesses sufficient stiffness to resist deformation under applied loads, and thus both displacement and rotation at the fixed end are assumed to be negligible. A cantilever beam model is established using the extended steel segment of the slider, the nylon base, and the U-shaped fork rod, as shown in Figure 2b.

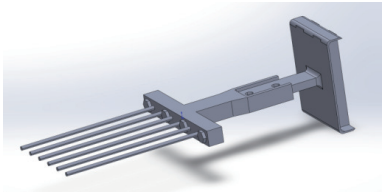

Figure 1 Three-dimensional model of the reciprocating vibration component

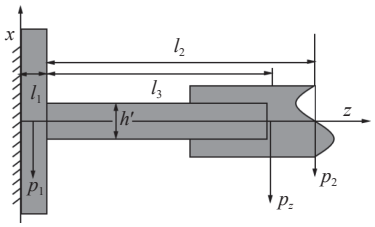

a. Overall model

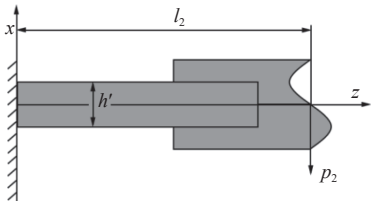

b. Simplified model

Figure 2 Schematic diagram of force distribution on cantilever beam

2.1.1 Determination of the stress function

As illustrated in Figure 2b, the cantilever beam is subjected to concentrated inertial forces. Employing the semi-inverse method and classical strength-of-materials theory, the Airy stress function φ' can be obtained. Clearly, the bending moment at any cross-section located at coordinate z is proportional to l_2–z, while the normal stress σ_z at a given cross-section is proportional to the x-coordinate of the acting point. Hence, we assume

$$\sigma_z = \frac{\partial^2 \varphi'}{\partial x^2} = c_1 (l_2 - z) x \tag{1}$$

Within the span of the beam, the stress function can be written as

$$\varphi' = \frac{c_1}{6} (l_2 - z) x^3 + x \left(c_2 z^3 + c_3 z^2 + c_4 z \right) + \left(c_6 z^3 + c_7 z^2 \right) \tag{2}$$

2.1.2 Determination of the stress components

The stress components corresponding to stress function (Equation (2)) are given by

$$\begin{cases} \sigma_x = \dfrac{\partial^2 \varphi'}{\partial z^2} = 6(c_2 x + c_6) z + 2(c_3 x + c_7) \\ \tau_{zx} = -\dfrac{\partial^2 \varphi'}{\partial z \partial x} = \dfrac{c_1}{2} x^2 - 3 c_2 z^2 - 2 c_3 z - c_4 \end{cases} \tag{3}$$

The constants c_1, c_2, c_3, c_4, c_5, c_6, c_7 are determined based on the boundary conditions. The loading form at the free end is unknown, but since it is a "small boundary", integral boundary conditions can be used as a substitute. The boundary condition expressions for this problem are:

$$\begin{cases} \sigma_z \left(z, \pm \dfrac{h'}{2} \right) = 0, \ \ \tau_{xz} \left(z, \pm \dfrac{h'}{2} \right) = 0 \\ \displaystyle\int_{-\frac{h'}{2}}^{\frac{h'}{2}} \sigma_z (l_2, x) \, \mathrm{d}x = 0, \ \ \int_{-\frac{h'}{2}}^{\frac{h'}{2}} \tau_{xz} (l_2, x) \, \mathrm{d}x = -P_2 \end{cases} \tag{4}$$

Combining the stress component expressions (1) and (3) with the upper and lower boundary conditions (4), it is evident that the boundary condition for σ_z at the free end is naturally satisfied according to the boundary conditions. The normal-stress requirement at the free end σ_z is automatically satisfied, giving the integration constants $c_2 = c_3 = c_6 = c_7 = 0$, $c_1 = P_2 / I_z$, and $c_4 = P_2 h'^2 / 8 I_z$, where I_z is the second moment of area of the cross-section, $I_z = b h'^3 / 12$. By substituting the integration constants into Equation (1) and Equation (3), the beam's stress components are obtained as follows.

$$\begin{cases} \sigma_z = \dfrac{P_2}{I_z} (l_2 - z) x \\ \sigma_x = 0 \\ \tau_{xz} = \dfrac{P_2}{2 I_z} \left(x^2 - \dfrac{h'^2}{4} \right) \end{cases} \tag{5}$$

The above expression is consistent with classical strength-of-materials formulas. Although the resultant force remains unchanged, the load at the free end no longer follows a parabolic distribution, so the derived equation is not entirely exact. However, when the stress concentration occurs at the far end of the beam, Saint-Venant's principle[24] suggests that Equation (4) remains applicable at distances from the end greater than the beam height h'. Furthermore, comparing the theoretical values with the simulation results in later sections shows that applying Saint-Venant's principle to approximate the stress distribution in this region of the cantilever beam effectively captures the key stress changes after loading, making it a suitable approximation for engineering applications.

2.1.3 Theoretical calculation

Assuming that both the slider and the extended connector are made of Al alloy, the vibration assembly comprises an Al-alloy extension handle, a nylon base, and a fork rod. The total mass m_b is 0.0775 kg, and the centroid is located 70.38 mm from the end of the Al handle. The cross-section of the Al extension handle is 15 mm in height and 5 mm in width.

Because the imposed vibrational acceleration is far greater than gravitational acceleration, the influence of gravity is neglected. The maximum inertial force acting on the vibration component depends on the amplitude and the motor speed. According to findings on the fruit-detachment mechanism, this force can be expressed as $F_{\max} = m a_{x\max} = m r \omega^2$. With an optimal operating amplitude of 15 mm and a motor speed of 1200 r/min, and using the total cantilever mass, the maximum inertial force under no-load conditions is calculated to be 18.36 N; thus the concentrated load is $P_2 = 18.36$ N, and the distance from the center of mass to the end of the handle is $l_2 = 70.38$ mm. Substituting these values into Equation (5) yields $\sigma_z = 6.89$ MPa. Due to the chamfer at the root, stress concentration will occur. According to the numerical experiment of stress concentration[25], the stress concentration factor is K_T=1.34, so $\sigma_{z\max} = K_T \sigma_z = 9.23$ MPa.

2.2 Energy-consumption theoretical model construction

According to our preliminary research findings[26], the crank driving torque and power of the reciprocating vibration component under no-load conditions are given by

$$\begin{cases} T_q = r \sqrt{\begin{aligned} &\left\{ \mu_1 \left[\mu_2 (m_2 + m_3) g \cos\varphi + 2\mu_3 \frac{m_3 g (s_1 + s_2) - m_2 g b_1}{h} + \right. \right. \\ &\left. \left. k' (r\omega \sin\omega t)^2 + (m_1 + m_2 + m_3) r \omega^2 \cos\omega t \right] + m_1 g \cos\varphi \right\}^2 + \\ &\left[\mu_2 (m_2 + m_3) g \cos\varphi + 2\mu_3 \frac{m_3 g (s_1 + s_2) - m_2 g b_1}{h} + \right. \\ &\left. k' (r\omega \sin\omega t)^2 - m_1 g \sin\varphi + (m_2 + m_3) r \omega^2 \cos\omega t \right]^2 \end{aligned}} \\ P = \dfrac{T_q \omega}{\eta} \end{cases} \tag{6}$$

where, T_q is the no-load torque acting on the vibration component, N·m; r is the crank length, kg; ω is the angular velocity of the crank about the origin, rad/s; η is the motor transmission efficiency; μ_1 is the rolling-friction coefficient between the crank-end bearing and the slider guide; μ_2 is the friction coefficient between the lower housing and the slider; m_2 is the mass of the slider, kg; m_3 is the mass of the linkage mechanism and fork rod, kg; g is the gravitational acceleration, taken as 9.8 m/s^2; φ is the angle between the vibration component and the horizontal x-axis, rad; μ_3 is the friction coefficient between the front and rear housings and the slider; s_1 is the distance from the centroid of the linkage and fork rod to the outer end of the linkage, m; s_2 is the y'-axis distance from the outer end of the linkage when it is hinged to the slider, m; b_1 is the y'-axis distance from the centroid of the slider, m; h is the height of the slider, m; k is the aerodynamic drag coefficient acting on the vibration component during operation; t is the rotation time, s; m_1 is the mass of the crank-end bearing, kg; P is the driving power of the motor under no-load conditions of the vibrating components, W; η is the transmission efficiency of the motor.

When a load is applied, the torque and power at the crank-end bearing of the reciprocating vibration component are given by

$$\begin{cases} T_{q'} = r\sqrt{\left\{\mu_1\left[\left(\dfrac{m_4gL_2r}{L_1^2}+k_2m_4r\omega^2\right)\dfrac{l_h+4\mu_3(s_2+s_3)}{l_h}\cos\varphi\cos\omega t+\right.\right.} \\ \left.\mu_2(m_2+m_3)g\cos\varphi+m_1g\cos\varphi+2\mu_3\dfrac{m_3g(s_1+s_2)-m_2gb_1}{h}+\right. \\ \left.k_1(r\omega\sin(\omega t+\epsilon))^2+(m_1+m_2+m_3)r\omega^2\cos\omega t\right]\Big\}^2+ \\ \left[\left(\dfrac{m_4gL_2r}{L_1^2}+k_2m_4r\omega^2\right)\dfrac{l_h+4\mu_3(s_2+s_3)}{l_h}\cos\varphi\cos\omega t+\right. \\ \left.\mu_2(m_2+m_3)g\cos\varphi+2\mu_3\dfrac{m_3g(s_1+s_2)-m_2gb_1}{h}+\right. \\ \left.k_1(r\omega\sin(\omega t+\epsilon))^2-m_1g\sin\varphi+(m_2+m_3)r\omega^2\cos\omega t\right]^2} \\ P' = \dfrac{T_{q'}\omega}{\eta} \end{cases} \tag{7}$$

where, $T_{q'}$ is the torque acting on the vibration component under load, N·m; m_4 is the mass of the branch, kg; L_2 is the distance from the branch's center of mass to the constrained end of the oscillating branch, m; L_1 is the distance from the contact point of the fork rod on the branch to the constrained end of the oscillating branch, m; k_2 is the correction coefficient for the overall inertial force of the branch under forced vibration; l_h is the length of the slider, m; s_3 is the distance from the branch–fork contact point to the outer end of the linkage mechanism, m; k_1 is the composite aerodynamic drag coefficient accounting for high-speed branch motion during vibration harvesting; ϵ is the phase lag of the branch's reciprocating swing velocity, rad; P' is the driving power of the motor under loaded conditions of the vibrating components, W.

3 Simulation analysis and topology optimization of the reciprocating vibration component

3.1 Simulation analysis of the reciprocating vibration component

Static analysis was conducted on reciprocating vibration components under no-load and loading conditions, respectively. The six degrees of freedom at the root surface of the reciprocating vibration components were constrained as boundary conditions. Based on our preliminary investigations, optimal operational parameters[26] were selected (amplitude of 15 mm and motor speed of 1200 r/min), with corresponding inertial forces (18.36 N) and applied loads (47.37 N) acting on the components serving as the loading conditions. The resulting stress distribution under no-load conditions is shown in Figure 3a, and the distribution under load conditions is shown in Figure 3b.

Using the same method, the stresses under no-load and load conditions at motor speeds of 1100 r/min and 1300 r/min were calculated; detailed data are provided in Table 1.

Al alloys and steels were initially considered as candidate materials for the slider. According to theoretical calculations, simulation results, and literature data, the minimum allowable stress for the 6061–6030 Al series ranges from 40 to 90 MPa. Under load conditions, the stress at the Al slider's concentration zone exceeds this minimum allowable value, yet remains well below the minimum allowable stresses for common steels—304, 316, 321, and 2205 stainless steels, as well as 45 carbon steel—which are 137.9 MPa, 130 MPa, 112.4 MPa, 207.5 MPa, and 180 MPa, respectively. Hence, Al alloys are unsuitable. The observed steel stress fracture indicates inadequate welding quality; therefore, steel should be selected as the slider material, and the welding process must be reinforced to ensure the reliability of the reciprocating vibration component.

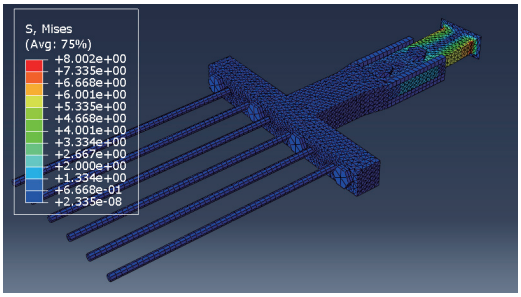

a. No-load

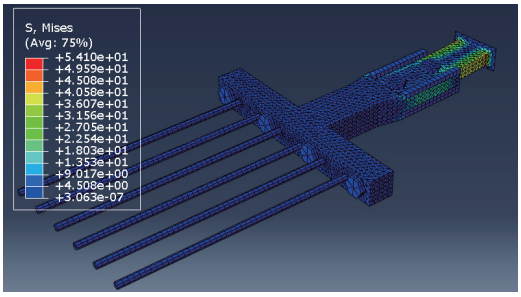

b. Load

Note: motor speed, 1200 r/mm; amplitude, 15 mm; simulated using Abaqus software.

Figure 3 Strain contour plot of the reciprocating vibration component

Table 1 Maximum stress of the reciprocating vibration component under various motor speeds and load conditions

Speed/ r·min^{-1}	No-load		Load	
	Theoretical value/MPa	Simulation value/MPa	Theoretical value/MPa	Simulation value/MPa
1100	7.76	6.72	47.30	45.46
1200	9.23	8.00	56.29	54.10
1300	10.84	9.39	66.07	63.50

Note: Amplitude is 15 mm.

3.2 Optimization of the reciprocating vibration component

Theoretical analysis shows that the reciprocating vibration component is subjected to inertial forces, and its mass has a substantial impact on those forces. Therefore, structurally optimizing the component to reduce its mass is an effective way to lower the inertial load. The component mainly consists of a slider, a nylon base, and a U-shaped fork rod, with the slider accounting for 57.24% of the total mass. Consequently, optimizing the slider can greatly reduce the overall mass. Moreover, to meet harvesting requirements, the nylon base and U-shaped fork rod are difficult to optimize, so the slider is chosen as the optimization target for the reciprocating vibration component.

3.2.1 Mathematical model for topology optimization in Abaqus

This study employs a topology-optimization strategy in Abaqus based on the Solid Isotropic Material with Penalization (SIMP) method. Taking minimum compliance as the objective and constraining the volume fraction, the optimization iteratively refines the structure in line with the loading characteristics of the vibration component. Within the SIMP framework, the elastic modulus is typically defined as

$$E(\rho) = E_{\max}(\rho^p + \rho_{\min}) \tag{8}$$

where, $E_{\max}$ is the elastic modulus of the solid material ($\rho = 1$); $\rho(x)$

is the material density variable at position x; p is the penalization factor that drives the element's relative density toward 0 or 1; ρ_{min} is a lower density bound introduced to prevent numerical singularities.

In this interpolation scheme, elements with densities approaching 1 have stiffnesses close to that of the solid material, whereas elements with densities approaching 0 behave almost like "voids". A higher penalization factor encourages densities to converge toward either 0 or 1, thereby producing a clearer, more distinct topology boundary.

In practical applications, minimizing compliance (for an elastic medium, equivalent to maximizing structural stiffness) is often adopted as the objective function, expressed as

$$\min_{\rho(x)} C(\rho,u) = \frac{1}{2}\int_{\Omega} \sigma(x) : \varepsilon(u(x))\,\mathrm{d}\Omega \tag{9}$$

where, $C(\rho,u)$ is the compliance, u is the displacement field of the structure under external loads, Ω is the design domain in which material may be distributed, and $\sigma(x) = D(\rho)\varepsilon(u(x))$, with $D(\rho)$ denoting the elasticity matrix associated with the material stiffness.

In addition to the objective function, the optimization problem typically includes a volume constraint and an equilibrium constraint. The volume constraint limits the amount of material in the final structure, while the equilibrium constraint ensures finite-element equilibrium. The constraints are expressed as

$$\text{s.t.} \begin{cases} F = K(\rho)u \\ V(\rho) = fV_0 = V_0 \\ 0 < \rho_{min} \le \rho < 1 \end{cases} \tag{10}$$

where, F is the nodal load vector; $K(\rho)$ is the global stiffness matrix dependent on ρ; $V(\rho)$ is the volume of the optimized structure; f is the prescribed volume fraction; V_0 is the volume of the design domain; ρ_{min} is a vector containing the minimum allowable relative density.

3.2.2 Topology optimization of the reciprocating vibration component

Topology optimization was performed by minimizing the strain energy of the slider while constraining the material volume to no more than 85% of the initial volume; the optimization outcome is shown in Figure 4a. Key structural features were extracted from the results, and—taking manufacturing cost and processability into account—the optimized slider was reconstructed in SolidWorks. The optimized slider weighs 48.5 g, representing a 38.61% reduction compared with the original 79 g. The optimized structure and the fabricated part are presented in Figure 4b and Figure 4c, respectively.

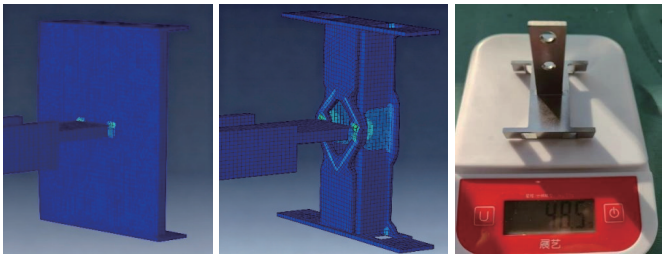

a. Pre-optimization model b. Post-optimization model c. Manufactured model

Note: Pre-optimization slider mass, 79 g; Post-optimization slider mass: 48.5 g; Structural simplification and manufacturing feasibility considered using Abaqus and SolidWorks software.

Figure 4 Comparison of the slider before and after topology optimization in the reciprocating vibration component

3.2.3 Safety factor and lifetime analysis of reciprocating vibration components

Based on the extreme operating conditions (torque is 0.69 N·m) during the best parameter test in the following section, a static structural simulation of the reciprocating vibration components was conducted using ANSYS 2022 to predict the safety factor and operational lifetime[27], as shown in Figure 5. The minimum safety factor of the reciprocating vibration component is 1.609, with the stress point enduring a minimum vibration count of 3.782×10^8, corresponding to a base rotational speed of 1200 r/min. The minimum continuous operating lifetime of the reciprocating vibration component is 5252 h.

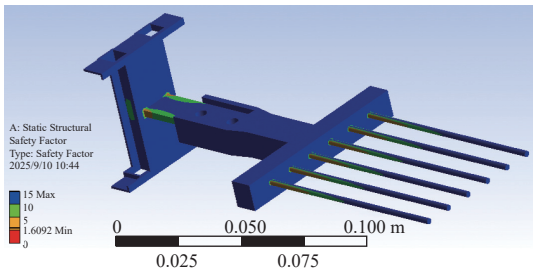

a. Safety factor

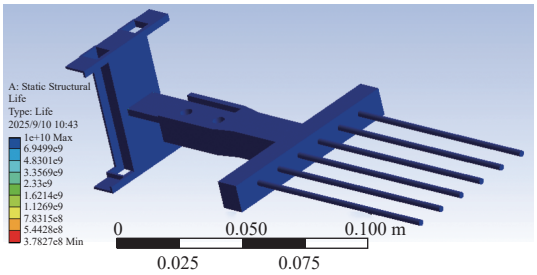

b. Lifetime

Note: load; motor speed, 1200 r/mm; amplitude, 15 mm; simulated using Ansys software.

Figure 5 Safety factor and lifetime simulation analysis of reciprocating vibration components

4 Comparative experimental analysis

To determine whether the optimized slider meets practical operational requirements while reducing the power consumption of the drive motor, experiments were conducted on the optimized reciprocating vibration component. Torque and motor power were compared with those of the pre-optimization component.

Based on the research framework[26], the input parameters for the energy-consumption model under the optimal operating configuration are as follows: r=0.015 m, ω=125.6 rad/s, η=0.9, μ_1=0.02-0.08, μ_2=0.1-0.15, m_2=0.047, m_3=0.064, μ_3=0.1-10.15, s_1=0.1 m, s_2=0.02 m, b_1=0.005 m, h=0.056 m, m_1=0.008 kg, m_4=0.02 kg (average mass of a single Chinese wolfberry branch), L_1=0.183 m, L_2=0.217 m, l_h=0.05 m, s_3=0.13 m, φ=0 (vibration component perpendicular to the vertical for both simulation and experimental verification), k'=0.25, k_1=0.5, k_2=1, ϵ=0.785 rad.

4.1 No-load simulation analysis

On the basis of Equation (6) and the parameters listed above, data were computed and plots generated in Matlab 7.1 to obtain the variation trends of driving torque and power for the vibration component. Simulations were carried out at the optimum operating frequency of 20 Hz and amplitude of 15 mm to analyze the reciprocating vibration component before and after the mass reduction achieved by optimization.

The masses of the vibration component were measured before and after optimization, yielding m_2= 0.079 kg, and m_2= 0.047 kg, respectively, while m_3= 0.064 kg and all other parameters remained unchanged. Aerodynamic drag was neglected so as to isolate the influence of mass on torque; the results are shown in Figure 6. As shown in Figure 6, the heavier, pre-optimization reciprocating component exhibits a peak torque of 0.52 N·m, which, according to Equation (7), corresponds to a power requirement of 72.49 W. After optimization, the lighter component shows a peak torque of 0.42 N·m and a corresponding power demand of 58.55 W, representing a 19.23% reduction. These results demonstrate that increased component mass leads to higher driving torque and greater power consumption. Consequently, provided that structural strength and stiffness are preserved, reducing the mass of the reciprocating vibration component is an effective strategy for improving energy efficiency under forced-vibration conditions.

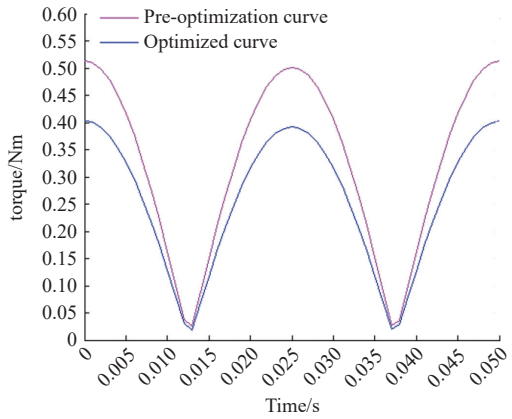

Note: No-load; Motor speed was 1200 r/mm; Amplitude was 15 mm; Simulated using Matlab software.

Figure 6 Effect of vibration component mass on torque under no-load conditions

4.2 Power consumption measurement system and experiment for the reciprocating vibration component

4.2.1 Construction of the reciprocating vibration component torque testing platform

Based on the simulation analysis conducted using the energy consumption model, and in response to speed and torque measurement requirements, a real-time torque detection platform driven by an AC servo motor was developed (system block diagram in Figure 7). A servo motor was selected as the power unit, and a high-precision torque sensor was installed between the output shaft of the AC servo motor and the vibration component, along with a corresponding signal filtering amplifier and an industrial data acquisition system. The platform allows for adjustable testing frequencies from 0 to 50 Hz, with the amplitude set to 15 mm.

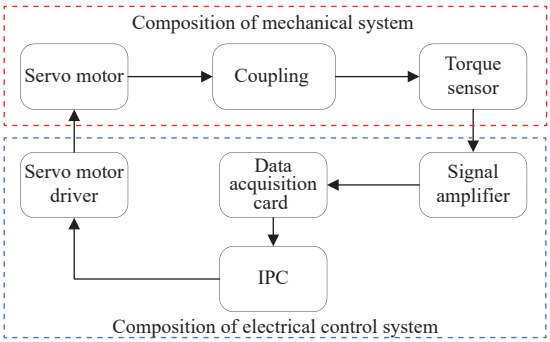

Figure 7 System block diagram of the testing platform

The real-time torque detection platform is composed of an AC servo motor, a torque sensor, a signal filtering amplifier, a data acquisition card, and control software. The overall system configuration is listed in Table 2. The AC servo motor is connected to the torque sensor via a coupling, and the sensor's output shaft provides the driving force to the vibration component. By measuring the torque variation at the output shaft of the servo motor, the platform provides a reliable method for practical torque detection and validation of theoretical results. The torque sensor transmits data via an RS-485 bus (using the MODBUS-RTU protocol) to the signal filtering amplifier, which processes the signal before transferring it to the upper computer through an RS-485 converter. The upper computer hosts an industrial signal measurement system composed of a USB DAQ-7606I data acquisition card and DAQsys management software. This setup constitutes the real-time torque detection platform shown in Figure 8 and Figure 9.

Table 2 Overall system configuration of the real-time torque detection platform

Component	Model	Main parameters or functions
AC servo motor	YELCHM 60Sm013030	Rated power: 400 W; Rated torque: 1.3 N·m (peak 5.73 N·m); Rated speed: 3000 r/min; Voltage: 220 V.
Torque sensor	CL1-202-2Nm	Range: 2 N·m; Output signal: 1.294 mV/V; Accuracy: 0.2% FS; Supply voltage: 5–12 VDC.
Signal amplifier	/	/
Data acquisition card	USB DAQ-7606I	USB 2.0 interface; Supports single measurement, point-based sampling, and continuous modes.
Management software	DAQsys	Centralized control of data acquisition devices; real-time waveform display, unit conversion, data storage, and waveform playback and analysis.

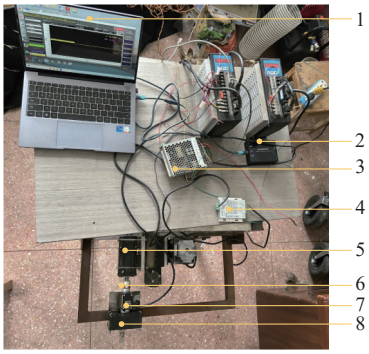

1. Upper Computer; 2. Data Acquisition Card; 3. Power Box; 4. Signal Amplifier; 5. Servo Motor; 6. Coupling; 7. Torque Sensor; 8. Vibration Component

Figure 8 Hardware composition of real-time torque detection platform

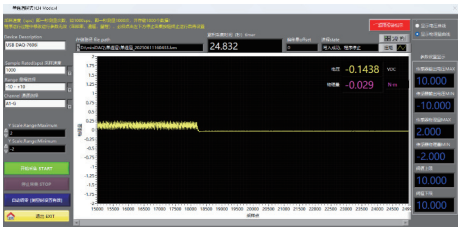

Figure 9 Signal measurement system of real-time torque detection platform

4.2.2 Torque detection test of reciprocating vibration components

Guided by the YELCHM motion-control platform, the actuator was excited at a nominal vibration frequency of 20 Hz. Torque signals were captured via the inline sensing module at 1 ms

intervals, yielding 50 discrete measurements per oscillatory cycle. The ensuing experiments were conducted as detailed below.

(1) Comparative analysis of no-load torque tests

Torque data under no-load operating conditions were collected using the torque sensing detection system. In this study, 100 data points from two full cycles were extracted, and the variation trend is shown in Figure 10.

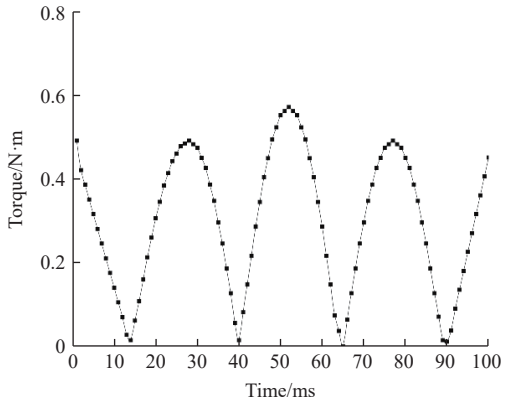

a. Pre-optimization

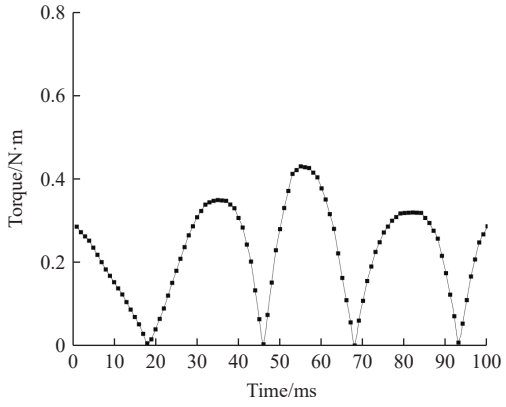

b. Post-optimization

Note: No-load; motor speed was 1200 r/mm; Amplitude was 15 mm; Experiments were conducted using a self-built torque measurement platform.

Figure 10 Torque variation profile under no-load conditions

To identify the peak torque output of the system, the data acquisition window was extended: 2000 data points were recorded over a 2 s interval, from which the top 20 peak torque values were selected for further analysis. A comparison of the maximum torque values before and after structural optimization of the reciprocating vibration mechanism is presented in Figure 11.

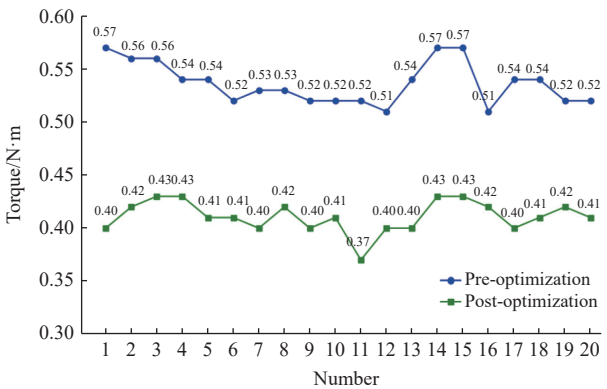

Figure 11 Extraction of actual maximum no-load torque for the reciprocating vibration component

As shown in Figure 11, the maximum torque prior to optimization reached 0.57 N·m, corresponding to a power output of 79.46 W. In contrast, the maximum torque after optimization decreased to 0.43 N·m, with a corresponding power output of 59.94 W, representing a 24.57% reduction in peak power consumption.

In the simulation analysis, the maximum no-load torque of the vibrating component prior to optimization was 0.52 N·m, while the corresponding experimental measurement yielded 0.57 N·m, resulting in a relative error of 9.62%. After optimization, the simulated torque was 0.42 N·m, and the experimentally measured value was 0.43 N·m, with a relative error of 2.38%. The close agreement between simulation and experimental results confirms the validity of the modeling and simulation approach. The reduced relative error observed after optimization is primarily attributed to the application of lubricant on the slider during actual testing, which reduced friction and consequently lowered the measured torque.

(2) Comparative analysis of loaded torque tests

Based on the conditions and findings of the no-load tests, five sets of Chinese wolfberry branches with masses of 20 g, 60 g, 100 g, 140 g, and 180 g were prepared. To examine the influence of loading on torque while considering data acquisition constraints, the central segment of each branch—ensuring consistent mass distribution during vibration—was selected for testing, as illustrated in Figure 12. For each group, torque measurements were collected using the same extraction method employed in the no-load experiments. The processed data are summarized in Figure 13.

Figure 12 Loaded torque experiment

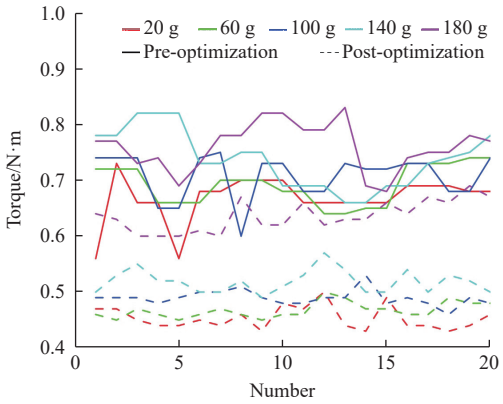

Figure 13 Extraction of actual maximum torque under varying loads

As presented in Figure 13, the maximum torque values measured under five different branch loading conditions before optimization were 0.73, 0.74, 0.75, 0.82, and 0.83 N·m, respectively. Correspondingly, after optimization, the maximum torque values recorded for the same loading conditions were 0.50,

0.50, 0.53, 0.57, and 0.69 N·m. According to Equation (7), the maximum driving power prior to optimization was 115.70 W, whereas after optimization it decreased to 96.18 W, representing a 16.87% reduction in peak power consumption.

Building on the preliminary experiments, the influence of load position and applied mass on torque was observed. Five sets of goji branches with masses of 20 g, 60 g, 100 g, 140 g, and 180 g were prepared. To ensure consistent vibration characteristics across the groups, the branches were subjected to loads applied at three different positions: 5 cm, 10 cm, and 15 cm from the base of the branch. For each group, torque measurements were taken using the same no-load data extraction method, and four full cycles of data were selected for comparison. The organized results are presented in Figure 14 and Figure 15.

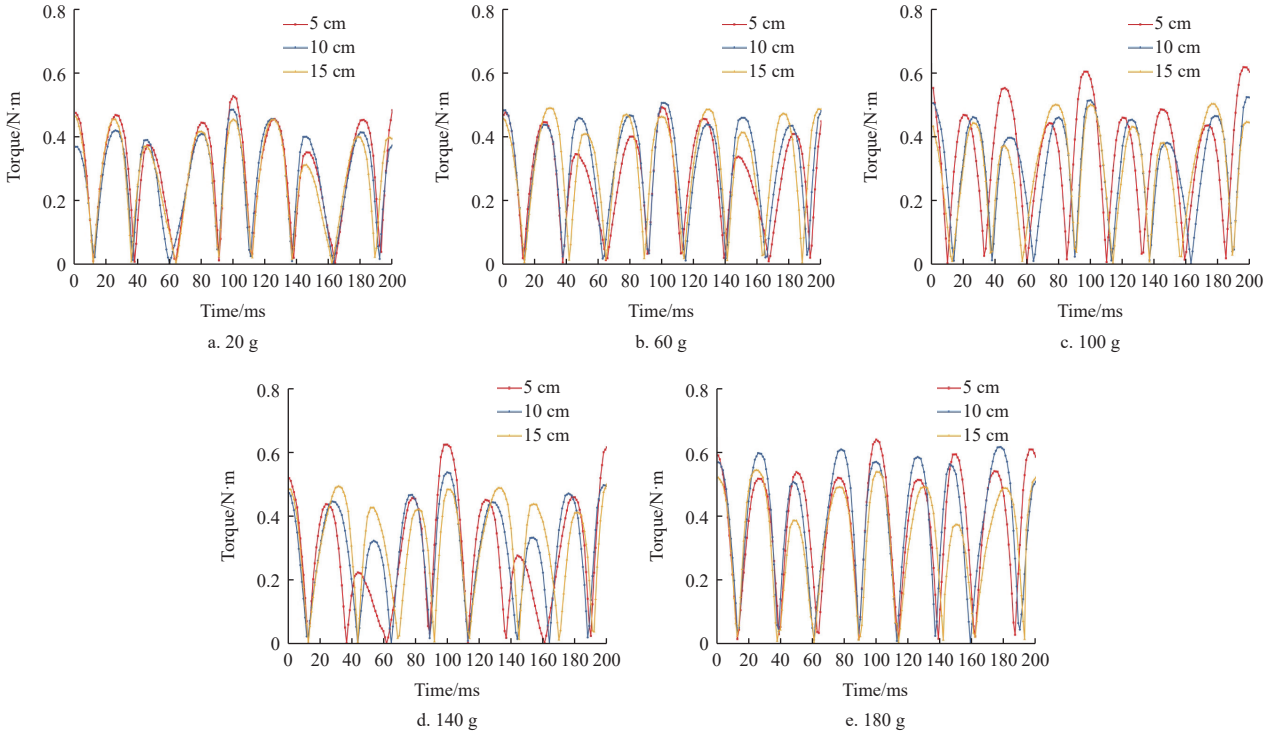

Figure 14 Torque comparison diagram under identical load at different positions

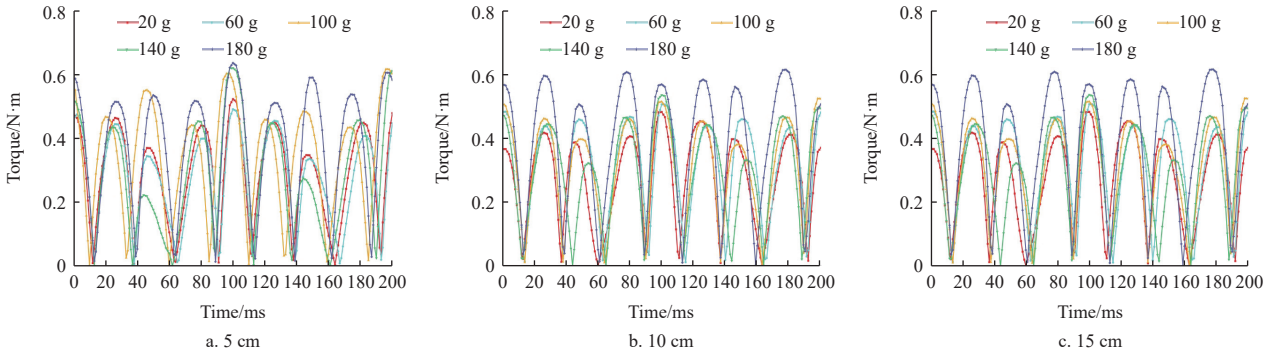

Figure 15 Torque comparison diagram under identical position with varying loads

As illustrated in Figure 14 and Figure 15, the following conclusions can be drawn: Under high-frequency, low-amplitude vibration conditions, the driving torque decreases as the operating position increases, while the driving torque increases with the increase in branch mass. The measured driving torque still meets the requirements of actual harvesting tasks, while the corresponding power consumption has significantly decreased. Therefore, the design of the vibration system must consider energy efficiency optimization under different load conditions, especially when there are significant variations in branch mass and operating position.

At the 5 cm position, relatively larger driving torque is often required. The maximum driving torque measured at 20 g, 60 g, 100 g, 140 g, and 180 g branch masses were 0.49, 0.53, 0.6, 0.62, and 0.64 N·m, respectively. These results were inconsistent with the simulation results shown in Figure 16a. Therefore, it was necessary to adjust the correction factor k_2 for the overall inertial force of the branch under forced vibration to match the actual driving torque. The calculated correction factors k_2 were 0.405, 0.184, 0.179, 0.131, and 0.104. The corrected actual driving torques are shown in Figure 16b.

At this point, the relationship between the branch load mass m_4 and the actual torque $T_{q'}$, as well as the relationship between the branch load mass m_4 and the correction factor k_2, were fitted. The first five polynomial terms were required to meet the specifications. For computational simplicity, a quadratic polynomial was chosen for the fitting, yielding the following results: $T_{q'} = -4.0179m_4^2 + 1.7786m_4 + 0.451\,18$, $k_2 = 15.4241m_4^2 - 4.7271m_4 + 0.4696$. The error values for these results were 0.018 205 and 0.072 34, respectively.

The fitted polynomial can be used to calculate and predict the actual driving power for load masses ranging from 20 g to 180 g, thereby determining the actual power consumption. For an experimental load mass of 60 g, the measured torque was 0.53 N·m, and the fitted calculation result was 0.543 N·m, with a calculated power of 75.71 W. For the maximum load mass of 180 g, the detected torque was 0.64 N·m, and the required power was 89.23 W. This process can be used to guide the selection of the driving motor under different load conditions. The model dynamically corrects the energy efficiency of vibration components under different load conditions, not only considering the power demands under operational states but also incorporating the impact of load on component efficiency. It provides a more precise basis for motor selection under various operational environments and load conditions.

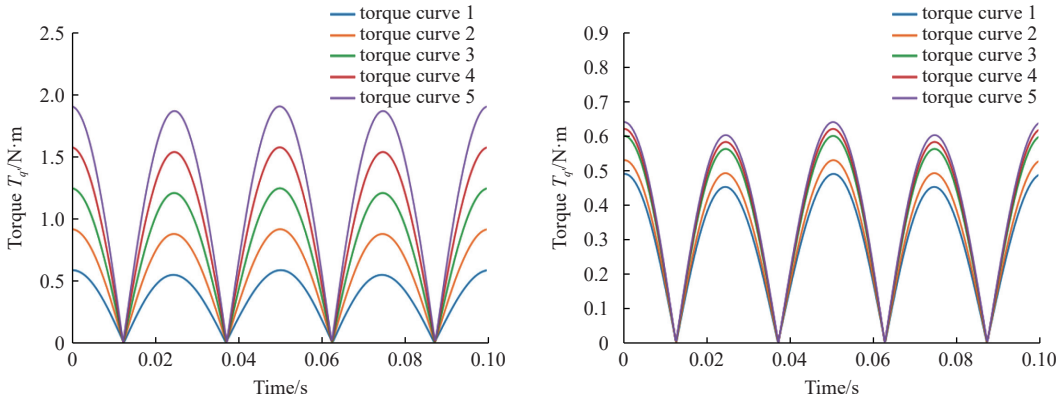

a.Torque simulation under different load conditions when k_2=1

b.Torque simulation under different load conditions after the correction of k_2

Figure 16 Impact of the branch forced vibration overall inertial force correction factor k_2 on torque simulation under different load conditions

5 Conclusions

Based on the operational mechanism and mechanical characteristics of reciprocating vibration components within vibratory Chinese wolfberry harvesting apparatus, this investigation examines the influence of diverse materials, structural parameters, and mass configurations on component stress distribution and power consumption through three analytical approaches: theoretical modeling, finite element simulation, and experimental validation. Furthermore, topology optimization and engineering-oriented design improvements were implemented for the slider components. The main conclusions are as follows:

(1) The theoretical cantilever beam model and finite element analysis consistently demonstrate that maximum equivalent stress concentrates predominantly at the junction between the slider extension shaft and the slider root connection. When aluminum alloy serves as the slider material, stress concentration regions exceed the corresponding minimum allowable stress under operational loading conditions, thereby compromising the durability requirements for sustained reciprocating vibration operations. Steel implementation as the material selection effectively mitigates such deficiencies; however, substandard welding specifications may precipitate fracture phenomena. Consequently, the adoption of steel materials coupled with enhanced critical welding processes constitutes a viable approach for ensuring the reliability of reciprocating vibration components.

(2) The inertial forces of reciprocating vibration components exhibit direct proportionality to component mass, whereby mass augmentation linearly escalates the demand for elevated driving torque and power requirements. Under the constraint of satisfying strength and rigidity specifications, mass reduction demonstrates the most pronounced impact on energy consumption reduction and operational efficiency enhancement, establishing lightweight design as the paramount strategy for energy optimization and performance improvement. Through topology optimization of the slider, supplemented by structural simplification and manufacturing feasibility considerations in SolidWorks, the actual designed slider achieved a mass reduction of 38.61% compared to the original configuration.

(3) Comparative analysis between no-load simulation and experimental results reveals that the pre-optimization component exhibited a simulated maximum torque of 0.52 N·m versus a measured value of 0.57 N·m, representing a deviation of 9.62%. Post-optimization values demonstrated a simulated torque of 0.42 N·m against a measured value of 0.43 N·m, with a deviation of merely 2.38%, significantly enhancing model accuracy. The lightweight design yielded approximately 24.6% and 16.9% reductions in driving torque and power consumption, respectively, relative to the original slider configuration. Maximum equivalent stress remained within acceptable safety margins under both no-load and various branch loading conditions, while driving torque and corresponding power requirements decreased substantially, validating that judicious structural optimization can simultaneously accommodate mass reduction and strength requirements.

(4) Based on experimental data, the relationship between the correction factor of the overall inertial force of branch forced vibration and load mass was fitted, leading to the development of the correction factor k_2 model. This improved the torque and power correction models under load conditions, revealing the variation patterns of load torque and power. The model can be used for predicting and selecting driving power within the load range of 20 g to 180 g. The proposed energy consumption correction model not only enhances prediction accuracy but also provides valuable guidance for motor selection, operational energy efficiency optimization, and overall performance improvement in vibration-based harvesters.

The lightweight design and energy efficiency optimization strategies proposed in this study have significant engineering application prospects. The lightweight design effectively reduces energy consumption and enhances operational efficiency, advancing

agricultural machinery towards higher energy efficiency. The energy consumption correction model provides a precise basis for motor selection, enabling optimized configurations based on operational conditions, reducing energy consumption, and extending equipment lifespan. Future research will focus on further optimizing energy efficiency models under multiple load conditions to improve adaptability in complex environments, while also exploring the integration of intelligent control systems in real-world applications, advancing the development of intelligent agricultural equipment.

Acknowledgements

This work is supported by the National Natural Science Foundation of China (Grant No. 32201681) and the Qinghai Province Science and Technology Program (Grant No. 2024-NK-141S-1).

[References]

[1] Zhou Z Q, Xiao J, Fan H X, Yu Y, He R R, Feng X L, et al. Polyphenols from wolfberry and their bioactivities. Food Chemistry, 2017; 214: 644–654.

[2] Wang J P, Mei S, Xiao H R, Zhao Y, Zhou H P. Research on mechanized harvesting methods of lycium barbarum fruit. IFAC PapersOnLine, 2018; 51(17): 223–226.

[3] Mei S, Shi Z G, Song Z Y, Wang R, Li Y. Present situation and development trend prediction of mechanized harvesting technology of Lycium barbarum. Agricultural Development & Equipments, 2021; 12: 12–14. (in Chinese)

[4] Wang Y T, Yang C, Gao Y Y, Lei Y Q, Ma L F, Qu A L. Design and testing of an integrated *lycium barbarum* L. Harvester Agriculture, 2024; 14(8): 1370–1384.

[5] Hu Y H, Feng J Z, Qiao Y C, Yu C H, Luo W K, Zhang K L, et al. Research and validation of vibratory harvesting device for red jujube based on ADAMS and ANSYS. Agriculture, 2023; 13(7): 1334–1357.

[6] Zheng Z Z, Hu Y H, Zhao P F, Dong J X, Huang Y X. Optimization and test of ripe-picking and green-leaving harvesting parameters for winter jujube catch-and-shake vibration device under facility orchard. Transactions of the CSAM, 2025; 56(1): 245–253. (in Chinese)

[7] Mei S, Wang J P, Song Z Y, Tang D B, Shen C. Mechanism and experimental study on the fruit detachment of chinese wolfberry through reciprocating vibration. Int J Agric & Biol Eng, 2024; 17(2): 47–58.

[8] Yang X, Jiang Z H, Li J P, Xie J Y, Gu H Y, Bian Y L. Simulation optimization and experiment of vibration parameters of apple picking by shaking branch processing. Transactions of the CSAM, 2024; 55(5): 28–39. (in Chinese)

[9] Ru Y, Fan G M, Xu L Y, Zhang H F, Zhou H P, Shi M H, et al. Design and vibration performance of a flexible rocker-arm walnut vibrating harvester. Scientia Silvae Sinicae, 2025; 64(4): 1–23. (in Chinese)

[10] Jang T Y, Tu Z J, Zhao J, Zhang J B. U-beam optimization design based on topology optimization. Journal of Highway and Transportation Research and Development, 2025; 42(2): 111–118. (in Chinese)

[11] Li Q, Yu Y Y, Xia F, Chen J Z, Wang Z G. Lightweight design of SPMT-mounted girder-carrying frame in overpass demolition based on topology optimization. World Bridges, 2024; 52(4): 15–21.

[12] Ma Y, Su W, Lai Q H, Zhang X, Yu Q X, Wan Y. Finite element analysis and topology optimization design of lightweight Panax Notoginseng transplanting machine frame. Journal of Intelligent Agricultural Mechanization, 2024; 5(2): 51–60. (in Chinese)

[13] Lu J. Optimization design and simulation analysis of the planetary gear reducer in hose reel irrigator. MS thesis, Zhenjiang: Jiangsu University, 2019; 6. 88p.

[14] Yang C L, Huang D M, Cheng F L. Finite element analysis and lightweight design of crusher flywheel. Applied Mechanics and Materials, 2014; 3615(684): 297–302.

[15] Arslan A M. Flywheel geometry design for improved energy storage using finite element analysis. Materials & Design, 2008; 29(2): 514–518.

[16] Zhao Y, Lan Y Z, Zhou Q, Shi S C, Zhai Z P. Static characteristics analysis and lightweight optimization of the rotor of straw crusher. Journal of Chinese Agricultural Mechanization, 2024; 45(9): 83–88.

[17] Liu H X, Yin L W, Xie Y T, Zhao Y J, Fang L. Development of the transfer platform with ground wheel in front for the medium-sized no-tillage stalk mulching ridge corn planter. Transactions of the CSAE, 2022; 38(10): 10–18. (in Chinese)

[18] Li M S, Wang Y J, Xie S Y, Liu Y F, Chen X Z, Li X, et al. Simulation analysis and test of the operation performance of shear vibration co-operation subsoiler based on discrete element method. Transactions of the CSAE, 2024; 40(20): 81–90. (in Chinese)

[19] Qi H K, Zhao J G, Liu C, Zuo Z, Ma Z K, Zhao Z X, et al. The optimization design and test of key components of the weeder between rows in corn field. Journal of Hebei Agricultural University, 2025; 48(1): 127–135.

[20] Zhu M J, Wu X H, Song Z H, Xie B, Wen C K, Chen S. Distributed hybrid electric tractor energy management strategy based on dual-layer optimization. Journal of Intelligent Agricultural Mechanization, 2025; 6(3): 1–10. (in Chinese)

[21] Xiao W, Lu J P, Deng C Y, Lin Z F. Research on power consumption model of sugarcane harvester cutting system based on ANSYS/Ls-Dyna. Journal of Chinese Agricultural Mechanization, 2022; 43(9): 116–121.

[22] Liu F P, Wu Z L, Yang Y, Liu Y F, Nie Y Z, Wu M L. Power analysis and simulation of rotary tillage for the rape seeding machine based on classical mechanics. Journal of Hunan Agricultural University (Natural Sciences), 2020; 46(3): 370–375.

[23] Zhu Y H, Xia J F, Zeng R, Zheng K, Du J, Liu Z Y. Prediction model of rotary tillage power consumption in paddy stubble field based on discrete element method. Transactions of the CSAM, 2020; 51(10): 42–50. (in Chinese)

[24] Toupin R A. Saint-venant's principle. Archive for Rational Mechanics and Analysis, 1965; 18(2): 83–96.

[25] Li H L. Numerical Experiment and Engineering Application of Stress Concentration. Northwest Hydropower, 2020; 51(10): 42–50. (in Chinese)

[26] Mei S, Tang D B, Shi Z G, Song Z Y, Shen C. Energy consumption mechanism simulation and experimental study of reciprocating vibration for chinese wolfberry picking. Int J Agric & Biol Eng, 2024; 17(4): 146–155.

[27] Jiang M S. Introduction and engineering practice of ANSYS Workbench 19.0. Beijing: People's Post and Telecommunications Press, 2019; 369P.